Magnetic LDH-based CoO–NiFe$_2$O$_4$ catalyst with enhanced performance and recyclability for efficient decolorization of azo dye via Fenton-like reactions

Akeem Adeyemi Oladipo[a,*], Ayodeji Olugbenga Ifebajo[b], Mustafa Gazi[b]

[a] *Cyprus Science University, Faculty of Engineering, Girne, North Cyprus via Mersin 10, Turkey*
[b] *Polymeric Materials Research Laboratory, Chemistry Department, Faculty of Arts and Science, Eastern Mediterranean University, Famagusta, North Cyprus via Mersin 10, Turkey*
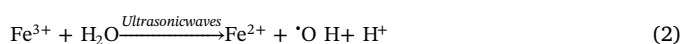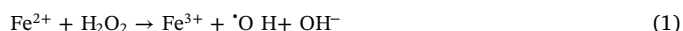
ARTICLE INFO

ABSTRACT

Magnetic CoO–NiFe$_2$O$_4$ catalyst was successfully fabricated from layered double hydroxide through a simple co-precipitation and calcination method, and for the first time applied as a novel Fenton-like catalyst for the de-colorization of Eriochrome black T dye (EB). The characteristics results demonstrated that CoO–NiFe$_2$O$_4$ exhibits a broad pore size distribution in the range of 5–40 nm, large specific surface area (363.6 m^2 g^{-1}) with the high structural stability and saturation magnetization (83.2 emu g^{-1}), hence, can be easily recycled for five sub-sequent runs without significant activity loss. The catalytic activity of CoO–NiFe$_2$O$_4$ was systematically eval-uated under varying reaction conditions including initial pH, catalyst dosage, initial dye and H$_2$O$_2$ concentra-tions. Under the optimal conditions, the CoO–NiFe$_2$O$_4$ accomplished ~87–97% decolorization of EB within 120 min. Here, the possible catalytic mechanism for EB decolorization is proposed and concluded to be multi-process induced by $^\cdot$OH, $^\cdot$O$_2$$^-$ or h^+ in the Fenton-like system.

1. Introduction

Nowadays, colours are often used in almost all manufacturing sectors and in fact are inseparable elements of human daily life. Even though the importance of dyes/colours to civilization is evident, the dye-polluted waters from the textile and allied industries are becoming a major source of environmental contaminations [1–3]. Untreated effluents from these industries make the water bodies become coloured and specifically distort the natural growth activity of aquatic life by blocking sunlight and stopping the re-oxygenation capacity of water [3–5].

The reactive azo dyes represent more than 50% of the global dye production due to their wide usage in dyeing industries, and also are the largest group of organic dyes containing —N═N— group as a chromophore in their structure [6–9]. Azo dyes are generally bio-resistant and persistent in the water bodies. Effluents containing even trace concentrations of azo dyes present hazardous effects [10,11]. Hence, efficient treatments are required to eliminate these potential toxic pollutants. Recent reports show that the advanced oxidation processes (AOPs) appear to be the most convenient and promising technique for the elimination of organic pollutants. The AOPs are able to rapidly and quantitatively mineralize bio-resistant organic compounds without producing secondary wastes [12–14].

Among the commonly used AOPs technologies, the Fenton and ultrasonic processes are effective and convenient treatment techniques widely applied for the removal of a variety of pollutants [8,10,15]. In the sono- and Fenton-AOP processes, hydroxyl radicals ($^\cdot$OH) are generated under ultrasonic waves and solar/UV irradiation, respectively. The $^\cdot$OH plays a major role in decolorizing dye polluted waters, specifically, it unselectively attacks organic pollutants and subsequently converts them to non-toxic inorganic species. The $^\cdot$OH is produced in the Fenton and sono-Fenton AOPs via the decomposition of H$_2$O$_2$/H$_2$O in the presence of Fe–based catalyst as expressed in Eqs. (1) and (2) [10,12,16]:

$$Fe^{2+} + H_2O_2 \rightarrow Fe^{3+} + {}^\cdot O\,H + OH^- \tag{1}$$

$$Fe^{3+} + H_2O \xrightarrow{Ultrasonic\,waves} Fe^{2+} + {}^\cdot O\,H + H^+ \tag{2}$$

Although the heterogeneous catalysts have displayed good performance in the Fenton process [17,18], they still have some disadvantages such as poor stability of the catalysts due to continuous leaching of active metals during the operation, lower activities compared to the homogeneous Fenton catalysts and the quenching effect caused by excess H$_2$O$_2$ or Fe^{2+} [17–19]. Hence, to circumvent the limitations of the heterogeneous Fenton catalysts, Fenton-like catalysts with high activity, improved stability and great durability have received increasing

---

attention [14,19–22].

In this study, CoO–NiFe$_2$O$_4$ mixed metal oxide was synthesized from Co–Fe layered double hydroxides and used as a heterogeneous catalyst in a Fenton-like and sonocatalytic process for decolorization of simulated textile wastewater containing eriochrome black T (EB) as an azo dyestuff. In particular, the CoO–NiFe$_2$O$_4$ catalyst exhibited significantly lower metal leaching during operation, improved catalytic and adsorptive performance in Fenton-like reaction, maintained high dispersity, and was easily recovered via an external magnetic field.

To the best of the author's knowledge, this is the first study that utilized CoO–NiFe$_2$O$_4$ to decolorize azo dyes from dye effluent. To evaluate performance and efficacy of the CoO–NiFe$_2$O$_4$ in adsorption, Fenton-like and sonocatalytic processes; the effect of CoO–NiFe$_2$O$_4$ dosage, initial dye solution pH, competing inorganic ions, reaction time and H$_2$O$_2$ concentration was investigated. The results herein indicate that the efficiency of the as-synthesized CoO–NiFe$_2$O$_4$ outperformed conventional adsorbents and heterogeneous catalysts, also note that the catalyst exhibited stable activities over successive recycling runs with the minimal loss of efficiency.

2. Materials and methods

2.1. Materials

All chemical reagents are analytical grade (> 98.5%), and distilled water was used in all experiments as a solvent. The cobalt (II) nitrate hexahydrate (Co(NO$_3$)$_2$·6H$_2$O) and sodium hydroxide were purchased from Sigma-Aldrich (Germany). Iron (III) nitrate nonahydrate (Fe(NO$_3$)$_3$·9H$_2$O) and nickel (II) nitrate hexahydrate (Ni(NO$_3$)$_2$·6H$_2$O) were supplied by Carlo Erba reagents (Spain). Eriochrome black T (EB) dye (Molecular weight: 461.4, CI: 14645, class: azo dye, λ = 530 nm) was purchased from Sigma-Aldrich (Germany) and used without purification.

2.2. Preparation of CoO–NiFe$_2$O$_4$ catalyst

The Co–Fe LDH intercalated with nitrate ions was synthesized via a simple co-precipitation technique [14]. Afterwards, the synthesized Co–Fe LDH was doped with Ni^{2+} and calcinated to obtain mixed metal oxide catalyst. Briefly, 5 g of Co–Fe LDH was introduced into a reaction flask containing freshly prepared Ni(NO$_3$)$_2$·6H$_2$O (0.069 M) aqueous solution, then stirred for 3 h at room temperature. The resulting products (Co/Ni–Fe LDH) were filtered, washed several times with distilled water–50% ethanol solution and dried at 60 °C overnight. Dried Co/Ni–Fe LDH was calcined at 600 °C in a muffle furnace at a heating rate of 10 °C/min for 5 h, then cooled to room temperature for the transformation into CoO–NiFe$_2$O$_4$ mixed metal oxides-based catalyst. The CoO–NiFe$_2$O$_4$ was ground into powder and sieved to a uniform size (0.25 mm) for further use.

2.3. Characterization of CoO–NiFe$_2$O$_4$ catalyst and Co–Fe layered double hydroxide

The textural measurements of the samples were obtained via the adsorption-desorption isotherms collected with N$_2$ at −196 °C on an Autosorb analyzer (QuantaChrome, USA). The specific surface areas and pores distribution of the samples were determined using the Brunauer-EmmettTeller (BET) equation and the Brunauer-Joyner-Hallenda (BJH) equation, respectively. Powder X-ray diffraction (XRD) patterns of the samples were recorded using a D-8 Advance diffractometer (Bruker-AXS, Germany) operated at 40 kV with Cu Kα radiation at a wavelength of 1.542 Å. They were recorded at the 2θ angular range over the 10–80° with 2 s/step and the crystalline phases were identified using standard JCPDS files.

The chemical compositions and surface morphologies of the samples were estimated by a JSM-6390 scanning electron microscope (JEOL,

Japan), fitted with a detector for energy dispersive X-ray analysis (EDX). Fourier transform infrared (FTIR) spectra were recorded on an FTIR-8700 spectrophotometer (Perkin-Elmer, Japan) with a resolution of 4 cm^{-1} in the range of 4000–400 cm^{-1} using the KBr pressed disk technique. The ultraviolet–vis diffuse reflectance spectra (DRS) of the samples were recorded using a UV–2450 spectrometer (Shimadzu, Japan) by the standard Kubelka-Munk method. The thermogravimetric analysis (TGA) was performed using the TA thermal analyzer instruments (Q600 SDT, USA) with a heating rate of 10 °C min^{-1} under nitrogen gas. The magnetic properties of the samples were examined using a vibrating sample magnetometer (VSM, 7400-S, Lakeshore, USA) with an applied field sweeping between ± 10,000 Oe at room temperature.

2.4. Adsorption and catalytic decolourization experiments

The reaction solutions of EB dye were freshly prepared from the dye stock solution (500 mg L^{-1}) and all experiments were conducted in a 200 m L-stoppered Erlenmeyer flasks placed on a thermostated system with an agitation of 200 rpm. The adsorptive decolourization activity of CoO–NiFe$_2$O$_4$ was evaluated by using 50 mL of an aqueous EB textile dye (50–200 mgL^{-1}) and 0.025 g powder of the magnetic CoO–NiFe$_2$O$_4$ catalyst under constant stirring and varied solution pH (2–10) at 25 °C.

The Fenton-like decolourization efficiency of CoO–NiFe$_2$O$_4$ under different conditions was also investigated. The activity of CoO–NiFe$_2$O$_4$ catalyst to decolorize EB was tested by varying parameters such as amount of catalyst between 0.01 g and 0.05 g, concentration of H$_2$O$_2$ between 2 and 20 mM and temperature of the solution between 35 and 50 °C in the dark, under solar irradiation and in an ultrasonic bath (ultra ET1311, 40 kHz, ENDA products England). During the adsorptive and Fenton-like decolorization processes, 2 mL sample was withdrawn after each predetermined interval after the start of the experiments. The spent CoO–NiFe$_2$O$_4$ catalyst was separated from the reaction flask using an external magnet. The remaining EB solution was determined at its maximum absorbance wavelength (λ$_{max}$ = 530 nm) by a double-beam UV–vis spectrophotometer (T80 + PG Instruments Ltd., UK).

The leached metal ion concentrations in the catalyst were determined by an atomic absorption spectroscopy (Novaa 400, Germany). To investigate the stability and reusability of CoO–NiFe$_2$O$_4$ catalyst, the spent catalyst was separated from the resulting suspension by an external magnet at the end of the experiment. The separated CoO–NiFe$_2$O$_4$ was eluted by 0.01 M NaOH or 0.01 M HCl, then dried at 80 °C and reused repeatedly. To confirm the existence of reactive radical species (hydroxyl radical (˙OH), superoxide (˙O$_2$$^-$) and photogenerated holes (h^+)) during the Fenton-like reactions, the strong radical scavengers (t − BuOH, p − benzoquinone and sodium oxalate, respectively) were added into the solutions just before reaction at mole ratio of [radical scavenger]/[H$_2$O$_2$] = 0.5 [14]. The decolorization efficiency of EB was calculated using the following equation:

$$Decolourization\, efficiency\, (\%) = (1 - C_t/C_0) \times 100 \qquad (3)$$

Here, the C_0 (mg/L) and C_t (mg/L) are the initial concentration and concentration of EB at a reaction time t (min). The measurements were repeated three times; the results were reproducible within the experiments errors (± 3%) and average results reported herein.

3. Results and discussion

3.1. Structural, morphological and physio-chemical characterization

Fig.1a shows the N$_2$ adsorption–desorption isotherms measured for LDH (Co–Fe) and mixed metal oxide derived from LDH (CoO–NiFe$_2$O$_4$). As clearly seen, isotherms of both samples exhibited type IV in shape with H$_3$ hysteresis and large N$_2$ uptake at $p/p_o \geq 0.85$, which is typical of layered double hydroxide-based materials [23]. The H$_3$ loop suggests the presence of mesopores (2–50 nm) between the agglomerating
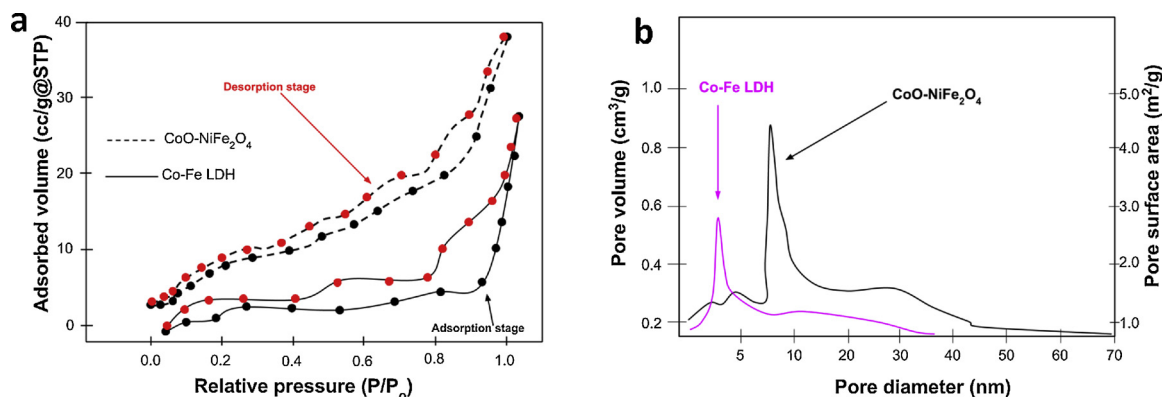
Fig. 1. a) N_2 adsorption/desorption isotherms of CoO–NiFe$_2$O$_4$ and Co–Fe LDH (b) Pore size distributions and pore surface areas of CoO–NiFe$_2$O$_4$ and Co–Fe LDH.

brucite-like particles with 3-dimensional interconnected pore geometry. It is observed that the N_2 quantities adsorbed onto CoO–NiFe$_2$O$_4$ were higher than that of Co–Fe LDH. Hence, CoO–NiFe$_2$O$_4$ possesses a larger specific surface area (363.6 m^2 g^{-1}) and a pore volume of 0.823 cm^3 g^{-1} compared with the Co–Fe layered double hydroxide (105.3 m^2 g^{-1} and 0.57 cm^3 g^{-1}, respectively). As indicated in Fig.1b, CoO–NiFe$_2$O$_4$ exhibits a broad pore size distribution in the range of 5–40 nm centred at about 9.5 nm with pore surface area of 4.65 m^2 g^{-1}. In contrast, the Co–Fe LDH displays a slightly narrower pore size distribution centred at 3.6 nm and pore surface area of 2.85 m^2 g^{-1}, suggesting that the CoO–NiFe$_2$O$_4$ internal mass transfer resistance for EB is comparatively negligible.

Fig. 2a displays the room temperature magnetic hysteresis loops of Co–Fe LDH and CoO–NiFe$_2$O$_4$. The results demonstrate the ferromagnetic behaviour of the samples and the corresponding values of the saturation magnetization (M_s = 83.2 emu/g), coercivity (H_c = 82.1 Oe) and remanence (M_r = 28.3 emu/g) of CoO–NiFe$_2$O$_4$ is higher than that of Co–Fe LDH (M_s: 61.3 emu/g, H_c: 41.3 Oe and M_r:16.3 emu/g). Apparently, the CoO–NiFe$_2$O$_4$ exhibited hard ferrites behaviour with high coercive field relative to the Co–Fe LDH. The partial introduction of Ni^{2+} into the Co–Fe LDH structure obviously enhanced the Ms value of the CoO–NiFe$_2$O$_4$ catalyst. This behaviour is consistent with the report of Oladipo et al. [24] and Naghshbandi et al. [25].

Fig. 2b shows the FT-IR spectra of Co–Fe LDH and CoO–NiFe$_2$O$_4$. The major peaks between 3800–3350 cm^{-1} in both samples correspond to the presence of −OH bond due to the stretching vibrations of adsorbed water and the interlamellar LDH structure [14,26]. As observed, the peak at 3484 cm^{-1} decreased in intensity and become narrower in the mixed metal oxide (3475 cm^{-1}), suggesting that the relative concentration of interlayered water molecules (δ–HOH) in the CoO–NiFe$_2$O$_4$ is decreased. The appearance of strong bands at 1360–1398 cm^{-1} is the NO$_3^-$ in the interlayer of the LDH structure [14,27]. Furthermore, the peaks in the range of 850–400 cm^{-1} can be interpreted as lattice vibration modes of M−O and M−OH. Specifically, the presence of Co–O, Fe–O and Ni–O was proven by the absorption peaks at 659, 565 and 450 cm^{-1} [27,28]. Apparently, the shift in the intensity of the IR absorption peaks of CoO–NiFe$_2$O$_4$ towards lower wave number compared with the pure Co–Fe LDH indicated the successful formation of the mixed metal oxide. After, adsorption and photocatalytic processes, no significant changes were observed in the FTIR of the samples.

From Fig. 3a, the Co–Fe LDH exhibit a characteristic hexagonal plate-like structure, which is typical for the layered double hydroxide morphology [14]. The observed plate-like structure may result from the rapid conversion of the aggregated Co(OH)$_2$ and Fe(OH)$_3$ particles into hydrotalcites, which is consistent with a previous report [29]. However, in the CoO–NiFe$_2$O$_4$ SEM image (Fig. 3b), it is observed that the plate-like structure of the Co–Fe LDH precursor collapsed partially after
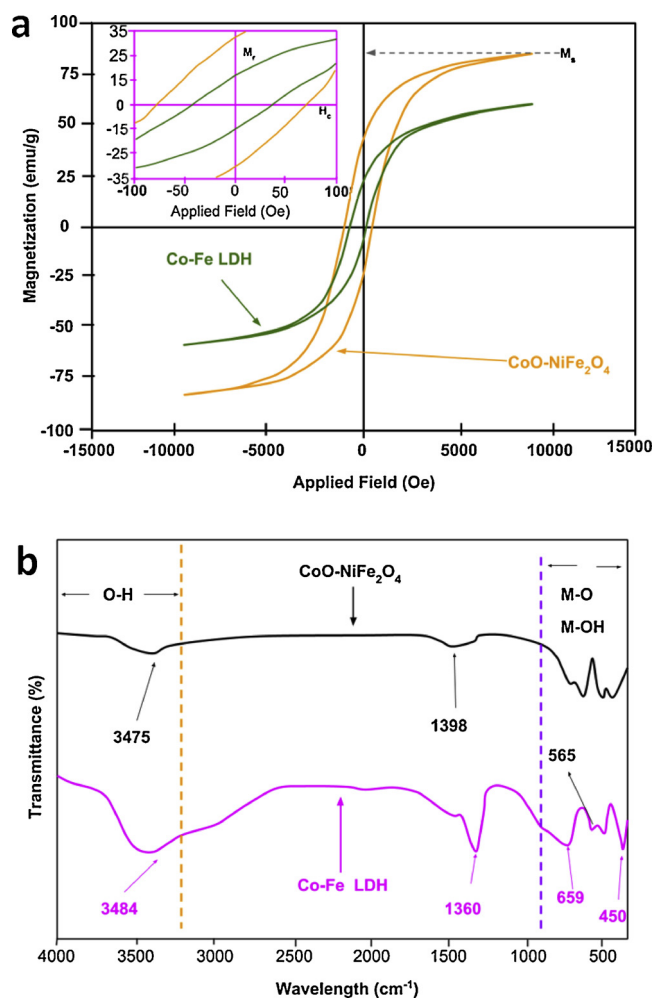

Fig. 2. a) Magnetic hysteresis loops for the samples, the inset shows the coercivity (Hc) and remanence (Mr) of the samples (b) FTIR spectra of the CoO–NiFe$_2$O$_4$ and Co–Fe LDH.

calcinated leading to the breaking away of brucite-like layers. Also, larger particles can be found in CoO–NiFe$_2$O$_4$, implying the growth of the introduced NiO on the surface of the aggregated CoO and Fe$_3$O$_4$ particles. Thus, the slight change in the morphology of the mixed metal oxide may influence its surface adsorption and photocatalytic properties. These analyses agree well with the XRD and EDX results of the CoO–NiFe$_2$O$_4$.

The energy dispersive X-ray mapping and point analysis were utilized to determine the chemical composition of the samples. The EDX
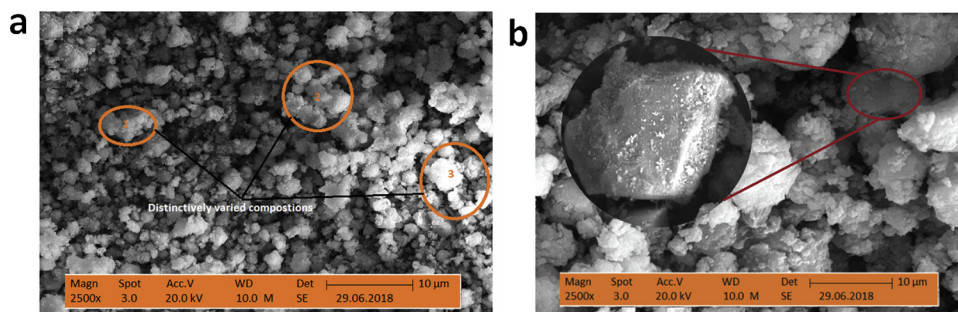
Fig. 3. SEM images of (a) Co–Fe LDH (b) CoO–NiFe$_2$O$_4$. Note that the compositions at the points numbered 1–3 in the selected region of the Co–Fe LDH vary distinctively from other regions.
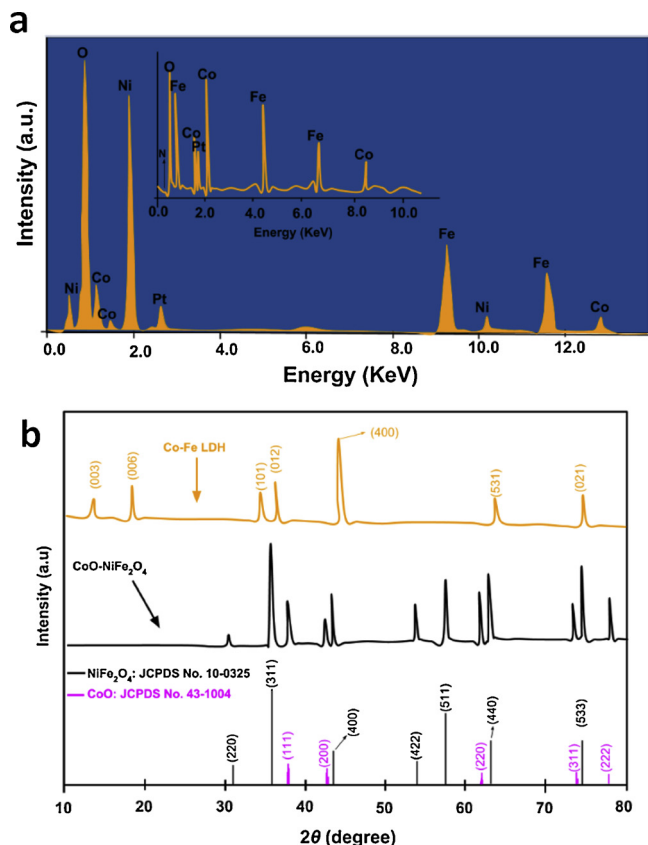

Fig. 4. a) Energy-dispersive X-ray of CoO–NiFe$_2$O$_4$ and Co–Fe layered double hydroxide (inset) (b) XRD patterns of the samples.

spectrum shown in Fig. 4a clearly indicates the presence of oxygen, iron, cobalt and nickel within the CoO–NiFe$_2$O$_4$ walls. Nickel ions are absent in the spectrum of Co–Fe LDH (Fig. 4a insert) and the results basically confirm the ratio of Co/Fe element is 3:1. However, the molar ratio of Co/Fe was found to reduce to 2.84 and Ni/Fe as 2.86 in the CoO–NiFe$_2$O$_4$. Thus, indicated that the nickel ions were inserted into the layered structure of the Co–Fe. Also, the elemental mapping by EDX reveals the non-uniformity of Co–Fe LDH. The distribution of Co and Fe elements in the selected regions of the SEM image varied distinctively. In particular, at points 1 and 3, the amount of Co and Fe is almost the same; in point 3, there is a significantly high concentration of Fe relative to Co; and the concentration of Co is a half of that for Fe at point 2 (Fig. 3a).

The crystal structures of the synthesized mixed metal oxide and Co–Fe layered double hydroxide are presented in Fig. 4b. The characteristic peaks of (003), (006), (101), (012), (400), (531) and (021) were obviously observed in the Co–Fe LDH sample, which indicates the

nature of nitrate intercalated LDH phase (JCPDS no. 50-0235) [29]. The obtained results indicated that the mixed metal oxide is composed of face-centred cubic CoO (JCPDS no. 43-1004) and cubic spinel structured NiFe$_2$O$_4$ that matches well with JCPDS card no. 10-0325. Specifically, the CoO exhibited diffraction peaks at 38.2°, 43.2°, 62.6°, 74.3° and 78.1° corresponding to (111), (200), (220), (311) and (222) lattice planes of the CoO. The typical NiFe$_2$O$_4$ reflections of (220), (311), (400), (422), (511), (440) and (533) planes were also observed in the mixed metal oxide. No impurity peaks were observed, which confirms the phase purity of all the samples. The crystallite size for the synthesized CoO–NiFe$_2$O$_4$ was calculated as 10.2 nm using Scherer formula ($D_s = 0.9\lambda/\beta \cos\theta$). Here, the λ is the X-ray wavelength, β is the full width at half-maximum intensity of the 311 reflections and θ is the Bragg diffraction angle.

The thermograms of the samples are presented in Fig. 5. The TGA curve of Co–Fe LDH exhibited typical thermal decomposition characteristics of LDH materials [30,31] with three distinct mass losses in the temperature ranges of 50–120 °C, 120–500 °C and 500–950 °C. The first mass loss was about 19%, which is attributed to the loss of interlayer and physically adsorbed water. About 8% weight loss was observed in the second step and can be attributed to the removal of nitrates from the interlayer and dehydroxylation of the LDH sheets [31]. Over this temperature range, the Co–Fe LDH underwent the first dehydroxylation. About 8.5% weight loss was observed at the third step, which is possibly due to further removal of nitrate ions, continuous dehydroxylation and formation of metal oxides. The TGA curve of CoO–NiFe$_2$O$_4$ catalyst indicated that it retained 86.5% of the initial mass. The apparent weight losses are in the range of 50–300 °C (12%) and 300–700 °C (1.5%), indicating complete removal of nitrate ions and the formation of spinel species (NiFe$_2$O$_4$) which are detected in the X-
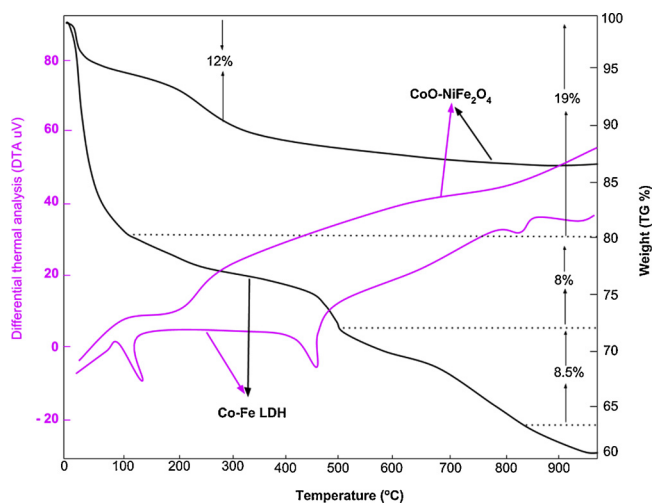

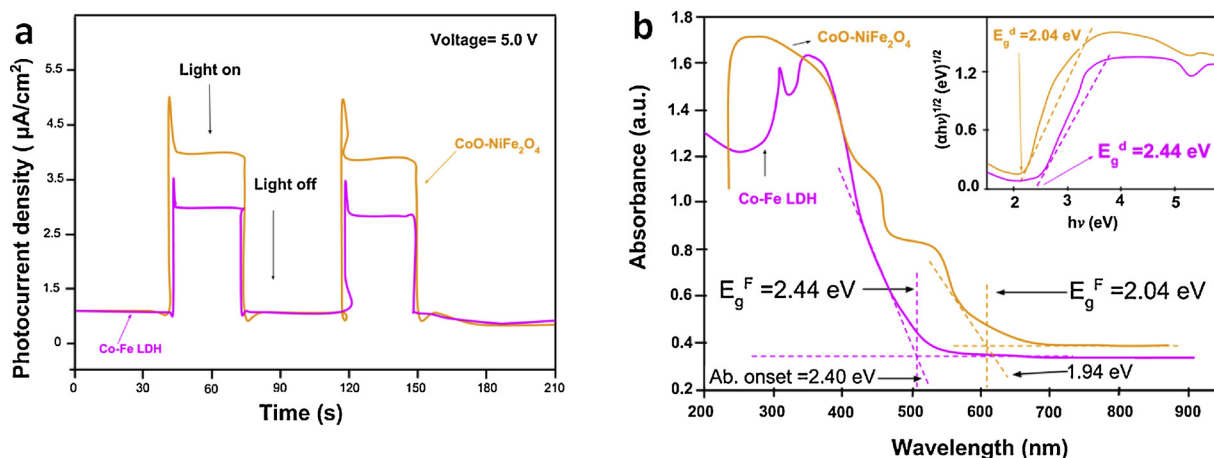**Fig. 5.** TGA and DTA of CoO–NiFe$_2$O$_4$ catalyst and Co–Fe layered double hydroxide.

Fig. 6. a) Transient photocurrent response of as-prepared samples (b) UV–vis spectra of CoO–NiFe$_2$O$_4$ catalyst and Co–Fe layered double hydroxide and the inset shows the band gap measurement of the prepared samples (Tauc plots).
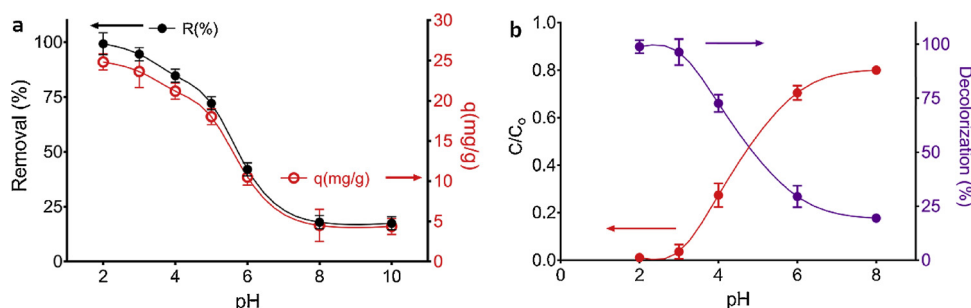

Fig. 7. Variation of solution pH on (a) Adsorptive removal of Eriochrome black T dye and (b) Fenton-like decolorization of EB by CoO–NiFe$_2$O$_4$. Reaction conditions; EB concentration: 50 mgL^{-1}, CoO–NiFe$_2$O$_4$ dosage: 0.025 g, volume of EB: 0.025 L, reaction time: 360 min and H$_2$O$_2$: 2 mmol L^{-1}.

ray diffractogram of CoO–NiFe$_2$O$_4$. As indicated in Fig. 5, the endothermic effects are obvious at 140 °C and 480 °C for Co–Fe LDH, which correspond to the removal of interlayer water and collapse of the brucite-like layer with the loss of interlayer NO$_3$– ions [32]. The TGA–DTA analyses confirmed that the ratio of weight loss in the Co–Fe LDH/CoO–NiFe$_2$O$_4$ is ~3.1%, which is justified by the amount of intercalated ions and interlayer water.

Fig. 6a depicted the transient photocurrent responses of Co–Fe LDH and CoO–NiFe$_2$O$_4$. The higher the photocurrent value, the more efficiently the photogenerated electron–hole pairs separate under identical operational conditions [12]. When the irradiation light turned on, the photo current rapidly increased for both samples, and then decreased to a constant value when the light was turned off. Obviously, the photocurrent for CoO–NiFe$_2$O$_4$ was much higher than those of Co–Fe LDH, indicating the more efficient separation of electron–hole pairs in CoO–NiFe$_2$O$_4$ [12,13]. The UV–vis spectrum of the samples is presented in Fig. 6b. It can be seen that the samples exhibited broad absorption in the range of 200–900 nm, suggesting that they absorb both UV and visible light [13].

The Co–Fe LDH and CoO–NiFe$_2$O$_4$ had an absorption onset threshold at approximately 516 nm and 639 nm, respectively. Compared to Co–Fe LDH, the CoO–NiFe$_2$O$_4$ exhibited stronger broad absorption and slightly red-shifted absorption edge in the visible region, which was ascribed to the coupling effect of CoO and NiFe$_2$O$_4$ components of the catalyst. The Tauc plots were constructed (Fig. 6b insert), assuming direct transitions ($n = 1$) in the equation $\alpha h\nu - A(h\nu - E_g)^{n/2}$ for both samples. Here, the E_g is band gap energy, A is constant, and h, α is Planck's constant and absorption coefficient, respectively. The specific absorption band energy (E_g) of each sample was estimated from $E_g = 1240/\lambda$, considering the direct absorption wavelengths at 607 nm and 508 nm, hence the E_g of CoO–NiFe$_2$O$_4$ and

Co–Fe LDH are 2.04 eV and 2.44 eV, respectively.

3.2. Adsorptive and catalytic performance of CoO–NiFe$_2$O$_4$ at different operational conditions

Adsorption and catalysis coexist in heterogeneous Fenton oxidation process [33,34]. Hence, the adsorptive performance of CoO–NiFe$_2$O$_4$ is important and consistent with the free radical driven mechanism of pollutants degradation over the catalyst surface. Essentially, the adsorptive porous surface of CoO–NiFe$_2$O$_4$ provides active sites to initiate H$_2$O$_2$ decomposition. Also note, the adsorbed pollutant molecules in the immediate vicinity of the active sites would be more easily attacked by the generated radicals [34,35].

3.2.1. Influence of initial pH

The pH point zero charge (pH$_{pzc}$) of CoO–NiFe$_2$O$_4$ was determined as 4.9 via the pH drift method [5], suggesting a positively charged surface at pH $<$ 5 [14]. The results in Fig. 7 indicated that the removal and decolorization efficiency of EB was significantly influenced by the solution pH. The optimal pH value for the removal of EB ($\sim$25 mgg^{-1}) achieved at pH 2.0 with 98.9% of decolorization of EB within 360 min reaction. The adsorption trend here is attributed to the combination of surface charge of the CoO–NiFe$_2$O$_4$ (pH$_{pzc}$ = 4.9) and pH-dependent speciation of EB (pKa values at 6.6 and 11.6) (Fig. 7a). Thus, EB molecules were negatively charged in the tested pH range. At highly acidic pH, the negatively charged EB molecules were attracted to the positively charged surface of CoO–NiFe$_2$O$_4$ resulting in highest removal capacity.

However, a minimum removal was established at pH greater than the pH$_{pzc}$ of the catalyst and pKa 6.6. At alkaline pH, two protons are dissociated from the EB, thus maximum repulsions occurred between
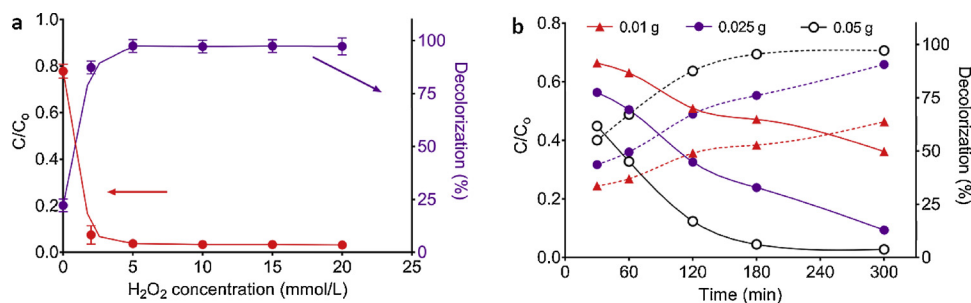
Fig. 8. Effects of (a) initial H_2O_2 concentration and (b) catalyst dosage on decolorization efficiency of EB (dashed lines). Reaction conditions were 0.025 g $CoO–NiFe_2O_4$, 50 mgL^{-1} EB, pH 2 and 300 min reaction time.

the more negatively charged EB and the negatively charged surface of $CoO–NiFe_2O_4$. Note that Fenton-like oxidation efficiency reduces with increasing solution alkalinity [36,37]. An important observation here revealed that the decolorization efficiency significantly reduced to 19.8% in the alkaline conditions in the presence of H_2O_2 (Fig. 7b). This may be due to the rapid conversion of ˙OH radicals to its less active conjugate base ˙O^- and eventually slows down the rate of decolorization of EB [18].

3.2.2. Influence of H_2O_2 concentration

In the Fenton-like system, the H_2O_2 plays the role of an oxidizing agent [33,38]. Obviously, the EB decolorization efficiency was increased from 22.2% to 94.5% with increasing H_2O_2 concentration from 0 to 5 mmol L^{-1}, and then remained constant when the H_2O_2 concentration was higher than 5 mmol L^{-1} (Fig. 8a). With the initial increase of H_2O_2 concentration to 5 mmol L^{-1}, the increased hydroxyl radicals enhanced the decolorization ability of the system. However, no significant effect was noticed beyond 5 mmol L^{-1}. This is likely due to the fact that excess amount of H_2O_2 could react with the ˙OH (H_2O_2 + ˙O H → ˙OOH + H_2O) to produce hydroperoxyl radical which exhibited relatively lower oxidation capability than ˙OH [18] and thus inhibited the decolorization efficiency of EB. A similar trend was also noticed in several other studies [19,21,39]. Based on the results here, 5 mmol L^{-1} was chosen as the appropriate H_2O_2 concentration for subsequent experiments.

3.2.3. Influence of $CoO–NiFe_2O_4$ dosage

As expected, the decolorization efficiency of EB increased with increasing $CoO–NiFe_2O_4$ dosage from 0.01 g to 0.05 g (Fig. 8b). It is observed that the highest decolorization efficiency (95.4%) was reached at the highest $CoO–NiFe_2O_4$ dosage, mainly because increasing the active sites of the catalyst can expedite the reactions to produce ˙OH, hence promoting the degradation efficiency of adsorbed EB [14,39]. Note that, the decolorization efficiency was found to be very fast for the initial 120 min followed by a slower rate from 120 to 300 min. The slow rate of decolorization beyond 120 min is likely due to the increases in the saturation of the adsorption sites with increasing reaction time since the decomposition of the EB molecules takes place on the surface of $CoO–NiFe_2O_4$ catalyst. Also, the decline in the dye concentration led to a slow rate of decolorization.

3.2.4. Influence of initial EB concentration

The effect of EB initial concentrations in the range of 50–200 mgL^{-1} on the decolorization rate was investigated at pH 2 using 0.05 g of $CoO–NiFe_2O_4$ and 5 mmol L^{-1} H_2O_2 in the dark. As presented in Fig. 9a, the decolorization efficiency of $CoO–NiFe_2O_4$ decrease with the increasing initial EB concentration within 300 min. The decolorization efficiency decreased from 90.6% to 54.4%, and decolorization rate decreased from 1.329 to 0.119 min^{-1} as the initial concentration of EB increased from 50 to 200 mg/L. Overall, high EB concentrations required a longer time to achieve decolorization. The decolorization of EB

occurred mainly by the reactions of ˙OH radicals with the −N≡N− bond of the azo dye with the generation of nitroso-aryl intermediates [40]. The low decolorization efficiency observed at high EB concentrations is due to the insufficient quantity of ˙OH in the reaction system while the number of EB molecules increases substantially at high concentrations, [˙OH] ≪ [EB] [41]. Hence, the generated ˙OH radicals are limited to attack the EB molecules under these experimental conditions.

3.2.5. Influence of temperature and inorganic ions on the decolorization of EB

The effect of reaction temperature on the decolorization of EB by $CoO–NiFe_2O_4$ is presented in Fig. 9b. Apparently after 60 min of catalytic oxidation, 93% and 68% decolorization efficiency were achieved at 50 °C and 35 °C, respectively. The results indicated that raising the temperature from 35 to 50 °C had a positive influence on the decolorization of EB, however, the decolorization rate increased more steadily when the solution temperature was maintained at 35 °C and no significant decolorization was observed beyond 120 min for both temperatures. Note that the higher temperature increased the reaction rate between $CoO–NiFe_2O_4$ and H_2O_2, and the generation rate of ˙OH radical increased simultaneously [42].

Also, the apparent activation energy (Ea) was calculated according to the logarithmic form of Arrhenius equation ($\ln k = (−E_a/RT) + \ln A$). where R denotes the universal gas constant, k represents the apparent rate constant, T represents the absolute temperature and A denotes to the pre-exponential factor. The Ea value was calculated as 46.8 kJ mol^{-1} and much higher than that of the diffusion-controlled reactions (10–13 kJ mol^{-1}), indicating that the EB decolorization process is not influenced by the mass transfer of EB but dominated by the chemical reaction occurring on the $CoO–NiFe_2O_4$ surface. In textile industries, high concentrations of various inorganic salts such as nitrate (NO_3^-), chloride (Cl^-) and sulfate (SO_4^{2-}) are often applied to enhance the dyeing rate of dyes. Here, the effects of these inorganic ions on the decolorization of EB demonstrated that the efficiency of $CoO–NiFe_2O_4$ is not hindered at high concentrations (0.2 mol L^{-1}) of NO_3^- and Cl^-. Note that the average decolorization rate of EB increased from 0.039 to 0.141 min^{-1} when the ions concentrations increased from 0 to 0.2 $molL^{-1}$. The formed ˙OH reacted with the ions to generate radicals (Cl˙ or ˙SO_4–) and thus enhanced the catalytic decolorization rate. The ˙Cl^- (1.36 V) and ˙SO_4^- (2.6 V) are oxidant species, however, are less reactive compared to the ˙OH radicals (2.72 V). It is worth mentioning that when the concentration of SO_4^{2-} was increased to 0.2 $molL^{-1}$, the decolorization rate decreased by 18%. At a very high concentration of SO_4^{2-}, the Fenton-like process weakened due to the hydroxyl scavenging properties of SO_4^{2-} and similar phenomenon reported elsewhere [43,44].

3.3. Comparative performance of processes for decolorization of EB

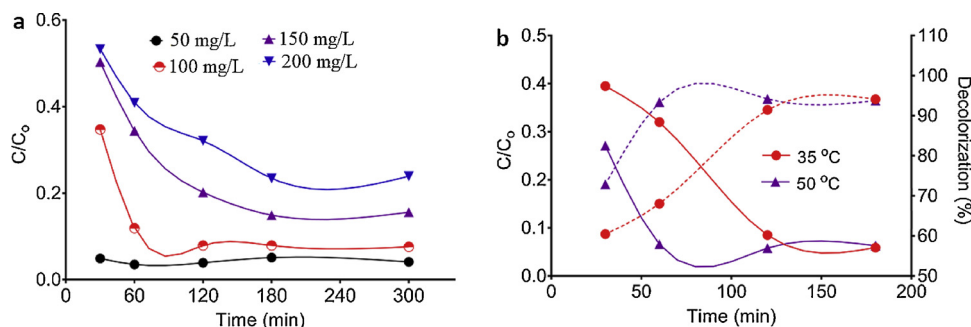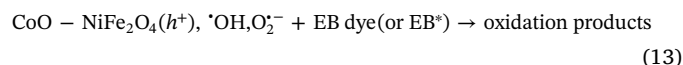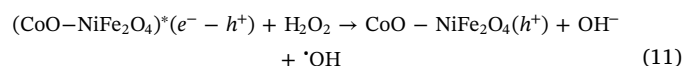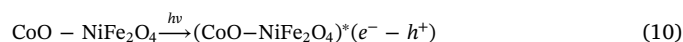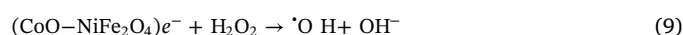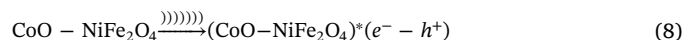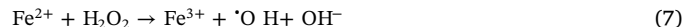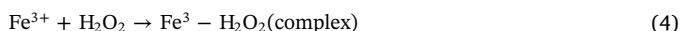Fig. 10a presents a comparison between the Fenton-like, photo-

Fig. 9. Effects of (a) initial EB concentration and (b) solution temperature on decolorization efficiency of EB (dashed lines). Reaction conditions were 0.05 g $CoO–NiFe_2O_4$, 5 mmol L^{-1} H_2O_2 and pH 2.

Fenton-like, sono-Fenton-like, adsorption and photolysis processes to explore the most effective system for EB decolorization. In these experiments, the solution pH is 2, 0.05 g $CoO–NiFe_2O_4$ was utilized and the concentrations of H_2O_2 was maintained at 5 mmol L^{-1} for the Fenton-like processes. It is observed that in the early stages of the reaction, the decolorization rate for the Fenton-like, photo-Fenton-like and sono-Fenton-like processes does not differ much. Notably, Fenton-like and photo-Fenton-like processes achieved nearly comparable decolorization efficiencies (61 and 67%, respectively) after a 30 min reaction time. However, as the reaction progresses, the photo-Fenton-like process increased the decolorization rate significantly and attained ~97% efficiency within the first 120 min. Thus, the obvious enhancement in the efficiency of EB decolorization in the photo-Fenton-like system is due to the synergistic effects of $CoO–NiFe_2O_4$–photocatalyzed oxidation and heterogeneous Fenton-like reaction.

The Fenton-like processes proceeded synchronously through various reaction steps described in Eqs. (4)–(13) [11,16,18,21,22]. Specifically, the interfacial Fe atoms in the structure of $CoO–NiFe_2O_4$ catalyst exist as Fe^{3+} ions with a remarkably high surface potential [45], hence can react with H_2O_2 to form $^{\cdot}OH$ radicals through the Fenton-like reactions in the dark (Eqs. (4)–(7)). For the sono-Fenton-like decolorization of EB, the ultrasound irradiation stimulated the $CoO–NiFe_2O_4$ with appropriate band gap energy to generate electron-hole pairs and the H_2O_2 captured the sono-induced electrons in the excited $CoO–NiFe_2O_4$ to form $^{\cdot}OH$ radicals (Eqs. (8) and (9)). In the photo-Fenton-like decolorization of EB, the photogenerated electron-hole pairs were formed on the surface of $CoO–NiFe_2O_4$ and the photogenerated electrons are trapped by the H_2O_2 to produce the $^{\cdot}OH$ radicals. The probable reaction steps involved in the photo-Fenton-like decolorization of EB are listed in Eqs. (10)–(13).

$$Fe^{3+} + H_2O_2 \rightarrow Fe^3 - H_2O_2 (\text{complex}) \tag{4}$$

$$Fe^3 - H_2O_2 \rightarrow Fe^{2+} + {}^{\cdot}OOH + H^+ \tag{5}$$

$$Fe^{3+} + {}^{\cdot}OOH \rightarrow Fe^{2+} + H^+ + O_2 \tag{6}$$

$$Fe^{2+} + H_2O_2 \rightarrow Fe^{3+} + {}^{\cdot}O\ H + OH^- \tag{7}$$

$$CoO - NiFe_2O_4 \xrightarrow{))))))))} (CoO–NiFe_2O_4)^*(e^- - h^+) \tag{8}$$

$$(CoO–NiFe_2O_4)e^- + H_2O_2 \rightarrow {}^{\cdot}O\ H + OH^- \tag{9}$$

$$CoO - NiFe_2O_4 \xrightarrow{hv} (CoO–NiFe_2O_4)^*(e^- - h^+) \tag{10}$$

$$(CoO–NiFe_2O_4)^*(e^- - h^+) + H_2O_2 \rightarrow CoO - NiFe_2O_4(h^+) + OH^- + {}^{\cdot}OH \tag{11}$$

$$CoO - NiFe_2O_4(e^-) + O_2 \rightarrow O_2^{\cdot -} \tag{12}$$

$$CoO - NiFe_2O_4(h^+), {}^{\cdot}OH, O_2^{\cdot -} + EB\ \text{dye (or EB*)} \rightarrow \text{oxidation products} \tag{13}$$

Also, note that the $CoO–NiFe_2O_4$ catalyst not only shows remarkable adsorption (78%) within the first 300 min but also exhibited significant photodecolorization (86%). The direct sunlight effect on the decolorization of EB was slightly greater than the darkness conditions in the presence of H_2O_2. This is attributed to the photolysis effect. In conclusion, these results confirmed that in all cases, the role of CoO–NiFe_2O_4 is fundamental for the decolorization of the EB solutions and the rates of decolorization were increased in the presence of optimum H_2O_2.

3.4. Identification of reactive oxidative species in the photo-Fenton-like reaction

To evaluate the photo-Fenton-like catalytic decolorization mechanism of the $CoO–NiFe_2O_4$, the key oxidative species were detected through radical trapping experiments using $p-$benzoquinone ($^{\cdot}O_2^{-}$ scavenger), sodium oxalate (h^+ scavenger) and $t-$BuOH ($^{\cdot}OH$ scavengers) [12]. As illustrated in Fig. 10b, the photocatalytic degradation of EB is obviously restrained after the injection of sodium oxalate and $p-$benzoquinone as the concentration of the scavengers increased from 5 to 20 mmolL^{-1}. It is observed that the addition of $t-$BuOH slightly
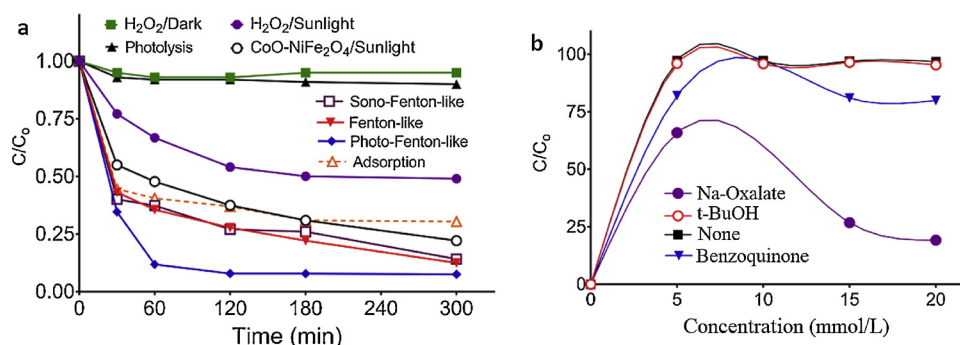

Fig. 10. a) Comparative performance of various processes for decolorization of EB (b) effect of different scavengers on the decolorization of EB in photo-Fenton-like reaction (initial H_2O_2 concentration = 5 mmol L^{-1}, initial pH = 2, $CoO–NiFe_2O_4$ = 0.05 g, and initial EB concentration = 50 mgL^{-1}).

decreased the photocatalytic degradation of EB by 1.1% when 20 mmol L^{-1} $t-$BuOH was added, suggesting that $\cdot$OH is not the main active species during the photocatalytic process. The EB decolourization was apparently inhibited after the addition of 20 mmolL^{-1} of $p-$benzoquinone and sodium oxalate, with the CoO-NiFe$_2$O$_4$ efficiency drastically decreased to 79.9% and 19.2%, respectively, suggesting that $\cdot$O$_2^-$ and h^+ had a major contribution for the EB photodegradation over CoO–NiFe$_2$O$_4$.

3.5. Photodecolorization mechanism of CoO–NiFe$_2$O$_4$

Thus, on the basis of the above results and previously reported studies, the photodecolorization mechanism of EB molecules by the magnetic CoO–NiFe$_2$O$_4$ mixed metal oxide catalyst under the visible light is proposed. The band gap energies of CoO, NiFe$_2$O$_4$ and CoO$-$NiFe$_2$O$_4$ were obtained as 2.52, 1.85 and 2.04 eV, respectively. The potentials of the conduction band (CB) and valence band (VB) for CoO and NiFe$_2$O$_4$, respectively, were calculated using the following empirical formulas [12]:

$$E_{VB} = \chi - E^e + 0.5E_g \tag{14}$$

$$E_{CB} = E_{VB} - E_g \tag{15}$$

Here, the E^e is the energy of free electrons on the hydrogen scale (4.5 eV); χ is the absolute electronegativity of the semiconductor (χ is 3.44 eV for CoO and 5.79 eV for NiFe$_2$O$_4$) and E$_g$ is the band gap of the semiconductor. The predicted CB and VB of CoO are -2.32 eV and 0.2 eV, while that of NiFe$_2$O$_4$ are 0.38 eV and 2.23 eV, respectively. Photocatalytic reaction proceeds due to electrons (e^-) and holes (h^+) generated in the photo-active materials by absorbing light energy [12,13]. As illustrated in Fig. 11, under visible light irradiation, the photogenerated e^- were excited from the VB to the CB, resulting in the formation of h^+ in the valence band of the photo-active materials.

Then, electrons in the CB of CoO could be transferred into the CB of NiFe$_2$O$_4$ because of the more positive CB of NiFe$_2$O$_4$ (0.38 eV) than that of CoO (-2.32 eV), which would be beneficial for decreasing the recombination of photogenerated holes$-$electrons pairs [30]. At the same time, the h^+ in the VB of NiFe$_2$O$_4$ were transferred to the VB of the CoO and thus act as the main active species in the oxidative degradation of EB, as supported by the trapping tests with h^+ and $\cdot$OH

radical scavengers. Hence, the photocatalytic degradation mechanism herein followed the path of typical heterojunction system and the remarkably increased photoactivity of the CoO$-$NiFe$_2$O$_4$ could be attributed to the efficient separation of the photoexcited electron–hole pairs.

According to the band edge position, the CB of the CoO is more negative than the reduction potential of O$_2$/$\cdot$O$_2^-$ (-0.33 eV vs. NHE). However, the CB of NiFe$_2$O$_4$ (0.38 eV) is more positive than O$_2$/$\cdot$O$_2^-$ (-0.33 eV), hence could not transform the O$_2$ into $\cdot$O$_2^-$. The photogenerated e^- at the CB of CoO directly reduced O$_2$ into $\cdot$O$_2^-$. This reduced $\cdot$O$_2^-$ can directly degrade the adsorbed EB into harmless intermediates or subsequently react with H$_2$O$_2$ in the system to produce $\cdot$OH which is suitable to degrade the EB. Similarly, the VB potentials of both CoO and NiFe$_2$O$_4$ were insufficient to generate $\cdot$OH radicals from the water molecule ($\cdot$OH /H$_2$O = 2.72 eV vs. NHE). This is consistent with the radical trapping results. Even though these VB levels could not produce hole mediated $\cdot$OH radicals, they could drag the holes and hence, contributed to the separation of electrons and holes [47]. Meanwhile, the $\cdot$OH generated from the CB of the CoO facilitated the degradation of the EB. In summary, by taking advantage of a combination of CoO and NiFe$_2$O$_4$, the probabilities of electron–hole recombination decreased significantly, and $\cdot$O$_2^-$ and h^+ can effectively degrade EB into CO$_2$, H$_2$O and other intermediates. Also, note that the amounts of oxygen are decreasing with the progress of the photo-Fenton-like catalytic process which confirms the degradation of the dyes during the process.

3.6. Kinetic of EB decolorization

The commonly used first-order degradation kinetic equation was applied to describe the kinetics of EB decolorization by CoO–NiFe$_2$O$_4$ under different Fenton-like processes. The kinetic equation is expressed here as [46]:

$$\ln \frac{C}{C_o} = -kt \tag{16}$$

Here, the C$_0$ and C (mg L^{-1}) are the initial concentration of EB in solution and after the reaction, respectively, k is the EB decolorization kinetic constant and t is reaction time (min). Two distinct stages of EB decolorization were identified in each process. The calculated
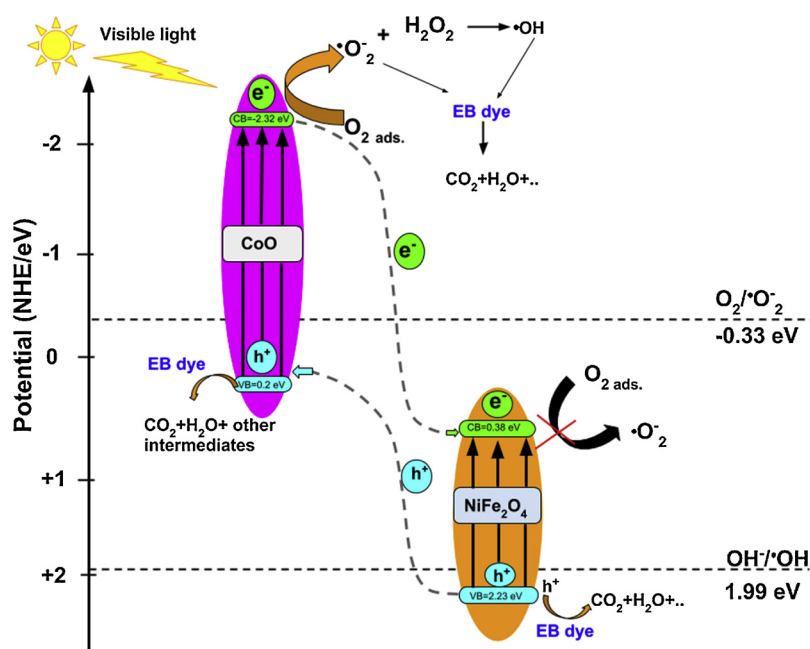

Fig. 11. Schematic representation of possible mechanism for the enhanced photo-Fenton-like reaction using CoO–NiFe$_2$O$_4$ as a heterogeneous catalyst.

Table 1
Decolorization kinetic constants and correlation coefficients (R^2) of EB under different processes.

Decolorization technique	Stage (time)	Equation	k(min^{-1})
Fenton-like	I (0–30 min)	Y= −1.021X + 0.016(R^2 = 0.968)	0.098
	II(30–240 min)	Y= −3.456X + 1.314(R^2 = 0.992)	0.139
Photo-Fenton-like	I (0–30 min)	Y= −2.341X + 1.516(R^2 = 0.993)	0.156
	II(30–120 min)	Y= −1.897X + 0.889(R^2 = 0.976)	0.102
Sono-Fenton-like	I (0–60 min)	Y= −1.893X + 0.345(R^2 = 0.987)	0.069
	II(60–180 min)	Y= −3.567X + 1.451(R^2 = 0.994)	0.149
Photolysis	I (0–30 min)	Y= −0.562X + 0.009(R^2 = 0.924)	0.056
	II(30–300 min)	Y= −0.978X + 0.046(R^2 = 0.958)	0.087

Initial concentration of EB: 50 mg L^{-1}.
CoO–NiFe$_2$O$_4$ dosage: 0.05 g.
pH: 2.
Temperature: 50 °C.

decolorization rate constants for EB are given in Table 1. For Fenton-like decolorization of EB, the first stage was slow followed by rapid decolorization (second stage). Specifically, the Fe^{3+} in the CoO–NiFe$_2$O$_4$ reacts with H$_2$O$_2$ to produce Fe^{2+} (Eqs. (4) and (5)) at a slow rate, which is reflected as a slow degradation of EB in the first step then followed by rapid decolorization by the generated ˙OH (Eq. (7)) in the second stage. The trend observed here confirms that the photo- and sono-degradation of EB dye obeyed pseudo-first order reaction kinetics. Similarly, Kansal et al. [48] revealed that EB photo-degradation by well-crystalline anatase TiO$_2$ nanoparticles followed pseudo-first order reaction kinetics with a rate constant of 0.017 min^{-1}.

3.7. Desorption, stability and reusability of CoO–NiFe$_2$O$_4$

The stability and reuse of the CoO–NiFe$_2$O$_4$ in the decolorization process was investigated by successive recycle experiments. First, desorption studies were performed using 0.01 M of either NaOH or HCl. Briefly, 0.025 g of EB-loaded CoO–NiFe$_2$O$_4$ was immersed in 25 mL desorption agent and agitated (200 rpm) for 60 min. The desorbed EB was determined by taking the absorbance values per cycle. As depicted in Fig. 12, it is observed that NaOH was a better desorption agent compared to HCl solutions. An average of ~75 and 98% desorption percentages were achieved during 6 consecutive desorption cycles by HCl and NaOH, respectively. Afterwards, the eluted CoO–NiFe$_2$O$_4$ was regenerated by drying at 80 °C and reuse for both adsorptive and Fenton-like decolorization treatment of 25 mg L^{-1} of freshly prepared EB solutions.

The performance of reusable NaOH eluted-CoO–NiFe$_2$O$_4$ did not change obviously after reusing six times for adsorptive removal of EB (~90–86%) compared with HCl (~29–56%). The slight loss of activity with NaOH eluted eluted-CoO–NiFe$_2$O$_4$ after successive recycling is

attributed to limited active sites due to blockage by adsorbed EB molecules. The efficiency of spent CoO–NiFe$_2$O$_4$ in the Fenton-like decolorization process demonstrated that CoO–NiFe$_2$O$_4$ maintained an acceptable catalytic activity with the EB decolorization efficiency of ~90% within 120 min in the sixth cycle, elucidating adequate reusability of CoO–NiFe$_2$O$_4$ for pollutants elimination. Here, we deduce that the loss of activity in the Fenton-like reuse experiments may be ascribed to the increasing consumption of the interfacial Fe atoms and less potential to convert excess H$_2$O$_2$ to reactive oxygen species for subsequent decolorization of EB.

The continuous leaching of metal ions is one of the direct causes of catalyst deactivation in the Fenton-like reactions. Here, the CoO–NiFe$_2$O$_4$ was submerged in aqueous solutions and the leached metal concentration was detected after 3 days to evaluate the stability of the catalyst. It is interesting to note that the concentration of leached iron, cobalt and nickel in the solution of CoO–NiFe$_2$O$_4$ is in the range of 0.04–0.53 mg L^{-1}, which is significantly lower than Fe-based catalysts reported elsewhere [14,49–51]. Also, the characteristic surface functional groups and phase composition of the recovered CoO–NiFe$_2$O$_4$ catalyst were almost same after consecutive use, confirming that CoO–NiFe$_2$O$_4$ is relatively stable.

3.8. Economic analysis of the treatment processes

Here, the economic analysis is discussed considering majorly the costs of the as-synthesized CoO–NiFe$_2$O$_4$ catalyst, chemicals (H$_2$O$_2$ and HCl) and electricity. According to Northern Cyprus electricity tariff (July 2018) and Sigma-Aldrich Chemicals, the costs of electricity is 2.2 US$ per 100 kW, CoO–NiFe$_2$O$_4$, H$_2$O$_2$ (30% Wt.) and HCl (37% w/v) are 29.5, 12.3 and 6.26 US$/kg respectively. The cost of each process is estimated herein considering the optimum treatment conditions (pH 2, EB concentration: 50 mg L^{-1}, H$_2$O$_2$: 5 mmol L^{-1}, treatment time: 60 min) and a fixed decolorization efficiency of 90%. For the sono-Fenton-like decolorization, the ultrasonic power consumption in 60 min per 1 m^3 wastewater treatment was obtained as 169 kW. Hence, the electricity cost for this process was 3.72 US$/m^3. The costs of catalyst and chemicals for the sono-Fenton-like process were obtained as 37.5 and 5.14 US$/m^3, respectively. Therefore, the total cost for treatment of EB polluted wastewater by this process was 46.36 US$/m^3. For Fenton-like and photo-Fenton-like (sunlight) treatment processes, 34.52 and 22.11 US$/m^3 were obtained respectively. Considering the high potential of CoO–NiFe$_2$O$_4$ and suitably high efficiency during five consecutive reuse cycles (< 95%), the cost of CoO–NiFe$_2$O$_4$ was divided by 3. As a result, the total costs of EB polluted wastewater treatment was obtained as 21.36, 16.45 and 9.56 US$/m^3 for sono-Fenton-like, Fenton-like and photo-Fenton-like processes respectively. Note that each process consumed different dosages of catalyst for the fixed decolorization efficiency. Overall, the ease of magnetic separation and recovery of CoO–NiFe$_2$O$_4$, its characteristics performance, low quantity of the H$_2$O$_2$ and the cost analysis, makes the Fenton-like treatment processes discussed herein comparatively suitable for industrial scale treatment of textile wastewater.

4. Conclusions

The new CoO–NiFe$_2$O$_4$ mixed metal oxide catalyst fabricated from layered double hydroxide exhibited ~97, 92 and 87% eriochrome black T dye decolorization via photo-Fenton-like, sono-Fenton-like and Fenton-like processes, respectively at optimum reaction conditions of 0.05 g CoO–NiFe$_2$O$_4$, 5 mmol L^{-1} H$_2$O$_2$, reaction time 120 min and pH 2.0. The characteristics results confirmed that CoO–NiFe$_2$O$_4$ exhibited a large specific surface area, ferromagnetic behaviour, and composed of face-centred cubic CoO and cubic spinel structured NiFe$_2$O$_4$. Effective decolorization was observed over a wider pH, however, the lowest decolorization efficiency at highly alkaline conditions is ascribed to rapid conversion of ˙OH radicals to its less active conjugate base ˙O$^-$.
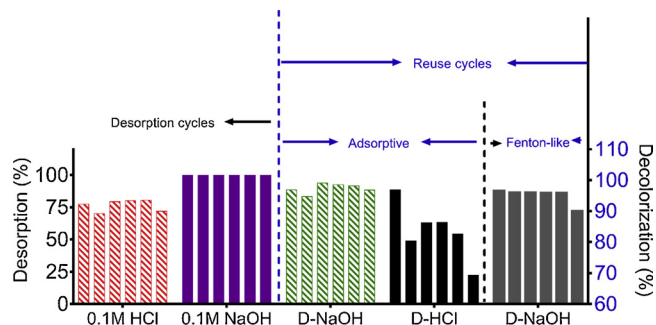

Fig. 12. Desorption efficiency and recyclability test of CoO–NiFe$_2$O$_4$ for adsorptive and Fenton-like catalytic activity.

The CoO–NiFe$_2$O$_4$ maintained stable catalytic activities, < 90% EB decolorization after five successive Fenton-like recycling oxidations. In summary, the enhanced photo-Fenton-like decolorization of EB by the CoO–NiFe$_2$O$_4$ is a complicated multiprocess and varieties of reactive species are involved such as $\cdot O_2^-$, h^+ and $\cdot OH$. Overall, CoO–NiFe$_2$O$_4$ demonstrated acceptable stability, superior catalytic activity and reusability in Fenton-like decolorization of azo dye at a comparably reasonable treatment cost (9.56–21.36 US\$/m^3).

References

[1] Z.G. Aguilar, E. Brillas, M. Salazar, J.L. Nava, I. Sirés, Evidence of Fenton-like reaction with active chlorine during the electrocatalytic oxidation of acid yellow 36 azo dye with Ir-Sn-Sb oxide anode in the presence of iron ion, Appl. Catal. B Environ. 206 (2017) 44–52.

[2] M. Shaban, M.R. Abukhadra, A.A.P. Khan, B.M. Jibali, Removal of Congo red, methylene blue and Cr(VI) ions from water using natural serpentine, J. Taiwan Inst. Chem. Eng. 82 (2018) 102–116.

[3] A.N. Ejhieh, M. Khorsandi, Photodecolorization of Eriochrome Black T using NiS–P zeolite as a heterogeneous catalyst, J. Hazard. Mater. 176 (2010) 629–637.

[4] A.A. Oladipo, M. Gazi, E. Yilmaz, Single and binary adsorption of azo and anthraquinone dyes by chitosan-based hydrogel: selectivity factor and Box-Behnken process design, Chem. Eng. Res. Des. 104 (2015) 264–279.

[5] A.A. Oladipo, M. Gazi, Microwaves initiated synthesis of activated carbon-based composite hydrogel for simultaneous removal of copper(II) ions and direct red 80 dye: a multi-component adsorption system, J. Taiwan Inst. Chem. Eng. 47 (2015) 125–136.

[6] F. Duarte, F.J. Maldonado-Hódar, A.F. Pérez-Cadenas, L.M. Madeira, Fenton-like degradation of azo-dye orange II catalyzed by transition metals on carbon aerogels, Appl. Catal. B Environ. 85 (2009) 139–147.

[7] A.A. Oladipo, Synthesis and Characterization of Modified Chitosan-based Novel Superabsorbent hydrogel: Swelling and Dye Adsorption behavior. Master's Thesis EMU, (2011) http://hdl.handle.net/11129/228.

[8] A.J. dos Santos, M.D. de Lima, D.R. da Silva, S. Garcia-Segura, C.A. Martínez-Huitle, Influence of the water hardness on the performance of electro-Fenton approach: decolorization and mineralization of Eriochrome Black T, Electrochim. Acta 208 (2016) 156–163.

[9] R.G. Saratale, G.D. Saratale, J.S. Chang, S.P. Govindwar, Bacterial decolorization and degradation of azo dyes: a review, J. Taiwan Inst. Chem. Eng. 42 (2011) (2011) 138–157.

[10] M. Karimi-Shamsabadi, M. Behpour, A.K. Babaheidari, Z. Saberi, Efficiently enhancing photocatalytic activity of NiO-ZnO doped onto nanozeoliteX by synergistic effects of pn heterojunction, supporting and zeolite nanoparticles in photo-degradation of Eriochrome Black T and Methyl Orange, J. Photochem. Photobiol. A Chem. 346 (2017) 133–143.

[11] M. Dindarsafa, A. Khataee, B. Kaymak, B. Vahid, A. Karimi, A. Rahmani, Heterogeneous sono-Fenton-like process using martite nanocatalyst prepared by high energy planetary ball milling for treatment of a textile dye, Ultrason. Sonochem. 34 (2017) 389–399.

[12] A.A. Oladipo, MIL-53 (Fe)-based photo-sensitive composite for degradation of organochlorinated herbicide and enhanced reduction of Cr (VI), Process Saf. Environ. Prot. 116 (2018) 413–423.

[13] A.A. Oladipo, R. Vaziri, M.A. Abureesh, Highly robust AgIO$_3$/MIL-53 (Fe) nanohybrid composites for degradation of organophosphorus pesticides in single and binary systems: application of artificial neural networks modelling, J. Taiwan Inst. Chem. Eng. 83 (2018) 133–142.

[14] A.O. Ifebajo, A.A. Oladipo, M. Gazi, Efficient removal of tetracycline by CoO/CuFe$_2$O$_4$ derived from layered double hydroxides, Environ. Chem. Lett. (2018), https://doi.org/10.1007/s10311-018-0781-0.

[15] A. Khataee, M. Sheydaei, A. Hassani, M. Taseidifar, S. Karaca, Sonocatalytic removal of an organic dye using TiO$_2$/Montmorillonite nanocomposite, Ultrason. Sonochem. 22 (2015) 404–411.

[16] M. Sheydaei, A. Khataee, Sonocatalytic decolorization of textile wastewater using synthesized γ-FeOOH nanoparticles, Ultrason. Sonochem. 27 (2015) 616–622.

[17] R. Idel-aouad, M. Valiente, A. Yaacoubi, B. Tanouti, M. Lopez-Mesas, Rapid decolourization and mineralization of the azo dye CI Acid Red 14 by heterogeneous Fenton reaction, J. Hazard. Mater. 186 (2011) 745–750.

[18] X. Shi, A. Tian, J. You, H. Yang, Y. Wang, X. Xue, Degradation of organic dyes by a new heterogeneous Fenton reagent - Fe$_2$GeS$_4$ nanoparticle, J. Hazard. Mater. 353 (2018) 182–189.

[19] N. Wang, T. Zheng, G. Zhang, P. Wang, A review on Fenton-like processes for organic wastewater treatment, J. Environ. Chem. Eng. 4 (2016) 762–787.

[20] M. Sheydaei, S. Aber, A. Khataee, Preparation of a novel γ-FeOOH-GAC nano composite for decolorization of textile wastewater by photo Fenton-like process in a continuous reactor, J. Mol. Catal. B: Chem 392 (2014) 229–234.

[21] M.Q. Cai, Y.Z. Zhu, Z.S. Wei, J.Q. Hu, S.D. Pan, R.Y. Xiao, C.Y. Dong, M.C. Jin, Rapid decolorization of dye Orange G by microwave enhanced Fenton-like reaction with delafossite-type CuFeO$_2$, Sci. Total Environ. 580 (2017) 966–973.

[22] Y. Liu, Q. Fan, J. Wang, Zn-Fe-CNTs catalytic in situ generation of H$_2$O$_2$ for Fenton-like degradation of sulfamethoxazole, J. Hazard. Mater. 342 (2018) 166–176.

[23] R. Xie, G. Fan, L. Yang, F. Li, Hierarchical flower-like Co–Cu mixed metal oxide microspheres as highly efficient catalysts for selective oxidation of ethylbenzene,
Chem. Eng. J. 288 (2016) 169–178.

[24] A.S. Oladipo, O.A. Ajayi, A.A. Oladipo, S.L. Azarmi, Y. Nurudeen, A.Y. Atta, S.S. Shola, Magnetic recyclable eggshell-based mesoporous catalyst for biodiesel production from crude neem oil: process optimization by central composite design and artificial neural network, C.R. Chim. 21 (2018) 684–695.

[25] Z. Naghshbandi, N. Arsalani, M.S. Zakerhamidi, K.E. Geckeler, A novel synthesis of magnetic and photoluminescent graphene quantum dots/MFe$_2$O$_4$ (M = Ni, Co) nanocomposites for catalytic application, Appl. Surf. Sci. 443 (2018) 484–491.

[26] G. Mendoza-Damián, F. Tzompantzi, A. Mantilla, R. Pérez-Hernández, A. Hernández-Gordillo, Improved photocatalytic activity of SnO$_2$–ZnAl LDH prepared by one step Sn^{4+} incorporation, Appl. Clay Sci. 121–122 (2016) 127–136.

[27] D. Chen, Y. Li, J. Zhang, J. Zhou, Y. Guo, H. Liu, Magnetic Fe$_3$O$_4$/ZnCr-layered double hydroxide composite with enhanced adsorption and photocatalytic activity, Chem. Eng. J. 185–186 (2012) 120–126.

[28] A.A. Oladipo, A.O. Ifebajo, Highly efficient magnetic chicken bone biochar for removal of tetracycline and fluorescent dye from wastewater: two-stage adsorber analysis, J. Environ. Manage. 209 (2018) 9–16.

[29] N. Rasouli, M. Movahedi, M. Doudi, Synthesis and characterization of inorganic mixed metal oxide nanoparticles derived from Zn–Al layered double hydroxide and their antibacterial activity, Surf. Interf. 6 (2017) 110–115.

[30] E. Abdelkader, L. Nadjia, B. Ahmed, Preparation and characterization of novel CuBi$_2$O$_4$/SnO$_2$ p–n heterojunction with enhanced photocatalytic performance under UVA light irradiation, J. King Saud Univ. Sci. 27 (2015) 76–91.

[31] J. Zhu, Z. Zhu, H. Zhang, H. Lu, Y. Qiu, L. Zhu, S. Küppers, Enhanced photocatalytic activity of Ce-doped Zn-Al multi-metal oxide composites derived from layered double hydroxide precursors, J. Colloid Interface Sci. 481 (2016) 144–157.

[32] R. Elmoubarki, F.Z. Mahjoubi, A. Elhalil, H. Tounsadi, M. Abdennouri, M. Sadiq, S. Qourzal, A. Zouhri, N. Barka, Ni/Fe and Mg/Fe layered double hydroxides and their calcined derivatives: preparation, characterization and application on textile dyes removal, J. Mater. Res. Technol. 6 (2017) 271–283.

[33] L. Gu, N. Zhu, H. Guo, S. Huang, Z. Lou, H. Yuan, Adsorption and Fenton-like degradation of naphthalene dye intermediate on sewage sludge derived porous carbon, J. Hazard. Mater. 246–247 (2013) 145–153.

[34] M. Gazi, A.A. Oladipo, Z.E. Ojoro, H.O. Gulcan, High-performance nanocatalyst for adsorptive and photo-assisted Fenton-like degradation of phenol: modeling using artificial neural networks, Chem. Eng. Comm. 204 (2017) 729–738.

[35] N.K. Daud, B.H. Hameed, Decolorization of Acid Red 1 by Fenton-like process using rice husk ash-based catalyst, J. Hazard. Mater. 176 (2010) 938–944.

[36] N.K. Daud, M.A. Ahmad, B.H. Hameed, Decolorization of acid red 1 dye solution by Fenton-like process using Fe–Montmorillonite K10 catalyst, Chem. Eng. J. 165 (2010) 111–116.

[37] F. Ji, C. Li, J. Zhang, L. Deng, Efficient decolorization of dye pollutants with LiFe(WO$_4$)$_2$ as a reusable heterogeneous Fenton-like catalyst, Desalination 269 (2011) 284–290.

[38] Z. Wan, J. Hu, J. Wang, Removal of sulfamethazine antibiotics using Ce–Fe-graphene nanocomposite as catalyst by Fenton-like process, J. Environ. Manage. 182 (2016) 284–291.

[39] Z. Li, X. Tang, K. Liu, J. Huang, Y. Xu, Q. Peng, M. Ao, Synthesis of a MnO$_2$/Fe$_3$O$_4$/diatomite nanocomposite as an efficient heterogeneous Fenton-like catalyst for methylene blue degradation, Beilstein J. Nanotechnol. 9 (2018) 1940–1950.

[40] M.Q. Cai, X.Q. Wei, Z.J. Song, M.C. Jin, Decolorization of azo dye Orange G by aluminum powder enhanced by ultrasonic irradiation, Ultrason. Sonochem. 22 (2015) 167–173.

[41] F.N.R. Quadrado, A.R. Fajardo, Fast decolorization of azo methyl orange via heterogeneous Fenton and Fenton-like reactions using alginate-Fe^{2+}/Fe^{3+} films as catalysts, Carbohyd. Polym. 177 (2017) 443–450.

[42] J.H. Sun, S.H. Shi, Y.F. Lee, S.P. Sun, Fenton oxidative decolorization of the azo dye Direct Blue 15 in aqueous solution, Chem. Eng. J. 155 (2009) 680–683.

[43] M. Xuhui, W. Lin, H. Song, Z. Hua, L. An, G. Fuxing, Enhanced electrochemical oxidation of phenol by introducing ferric ions and UV radiation, J. Environ. Sci. 20 (2008) 1386–1391.

[44] M.H. Farzana, S. Meenakshi, Exploitation of zinc oxide impregnated chitosan beads for the photocatalytic decolorization of an azo dye, Int. J. Biol. Macromol. 72 (2015) 900–910.

[45] Y. Soltanabadi, M. Jourshabani, Z. Shariatinia, Synthesis of novel CuO/LaFeO$_3$ nanocomposite photocatalysts with superior Fenton-like and visible light photocatalytic activities for degradation of aqueous organic contaminants, Sep. Purif. Technol. 202 (2018) 227–241.

[46] S. Yousefi-Mohammadi, M. Movahedi, H. Salavati, MnCo–Ferrite/TiO$_2$ composite as an efficient magnetically separable photocatalyst for decolorization of dye pollutants in aqueous solution, Surf. Interf. 11 (2018) 91–97.

[47] K. Goswami, R. Ananthakrishnan, S. Mandal, Facile synthesis of cation doped ZnO-ZnCo$_2$O$_4$ hetero-nanocomposites for photocatalytic decomposition of aqueous organics under visible light, Mater. Chem. Phys. 206 (2018) 174–185.

[48] S.K. Kansal, S. Sood, A. Umar, S.K. Mehta, Photocatalytic degradation of Eriochrome Black T dye using well-crystalline anatase TiO2 nanoparticles, J. Alloys Comp. 581 (2013) 392–397.

[49] J. Tang, J. Wang, Fenton-like degradation of sulfamethoxazole using Fe-based magnetic nanoparticles embedded into mesoporous carbon hybrid as an efficient catalyst, Chem. Eng. J. 351 (2018) 1085–1094.

[50] L.J. Xu, J.L. Wang, Fenton-like degradation of 2,4-dichlorophenol using Fe$_3$O$_4$ magnetic nanoparticles, Appl. Catal. B Environ. 123 (2012) 117–126.

[51] S.O. Ganiyu, M. Zhou, C.A. Martínez-Huitle, Heterogeneous electro-Fenton and photoelectro-Fenton processes: a critical review of fundamental principles and application for water/wastewater treatment, Appl. Catal. B Environ. 235 (2018) 103–129.